

# (Ni)MOF interpenetrated with MnO<sub>2</sub> nanothorns anchored on porous carbon cloth as self-standing cathode for high-performance supercapacitors

Jian Zou<sup>1,#</sup>, Yangyang Wang<sup>1,#</sup>, Zongyu Wang, Aiping Fu<sup>2</sup>, Yu-Guo Guo<sup>3,\*</sup>, Hongliang Li<sup>1,2</sup>,

<sup>1</sup> Institute of Materials for Energy and Environment, College of Materials Science and Engineering, State Key Laboratory of Bio-Fibers and Eco-Textiles, Qingdao University, Qingdao 266071, China

<sup>2</sup> College of Chemistry and Chemical Engineering, Qingdao University, Qingdao 266071, China

<sup>3</sup> Beijing National Laboratory for Molecular Sciences, Institute of Chemistry, Chinese Academy of Sciences (CAS), Beijing 100190, China

\* E-mail: [lhl@qdu.edu.cn](mailto:lhl@qdu.edu.cn)

# These two authors contributed equally to this work

Received: 8 May 2022 / Accepted: 9 June 2022 / Published: 4 July 2022

---

A composite of (Ni)MOF sheets penetrated by MnO<sub>2</sub> nano-nanothorns anchored on porous carbon cloth has been fabricated by a two-step hydrothermal method and been explored as self-standing electrode for high-performance supercapacitors. The composite delivers a high specific capacitance of 1780 mF cm<sup>-2</sup> at 4 mA cm<sup>-2</sup> (376 F g<sup>-1</sup> at 1 A g<sup>-1</sup> specific capacitance) and exhibits a capacitance retention of 93.4% at 15 mA cm<sup>-2</sup> after 5000 cycles. It reaches 71.6% of the original capacitance when the current density switches in between 4 and 15 mA cm<sup>-2</sup>, indicating an excellent rate capability. These results open up new avenues for the development of high-performance electrode materials and the application of advanced energy storage devices.

---

**Keywords:** MOF; MnO<sub>2</sub>; self-standing electrode; supercapacitor; porous materials

## 1. INTRODUCTION

The development of supercapacitors to replace conventional capacitors, batteries, and fuel cells has attracted considerable attention [1-3]. There are two different mechanisms for the generation of capacitance in supercapacitors. The first one is a double layer model in which electrons are physically adsorbed on the surface of a porous electrode [4,5]. Traditionally, the active materials for such a kind of supercapacitors are carbon materials with high specific surface area, such as activated carbon [6], carbon nanotubes [7] and graphene [8], and some metal oxides, such as RuO<sub>2</sub>[9], ZnO [10], MnCo<sub>2</sub>O<sub>4</sub>[11], NiO[12] and MnO<sub>2</sub>[13]. Among the transition metal oxides, MnO<sub>2</sub> shows a greater advantage owe to its

high theoretical specific capacity (about  $1370 \text{ F g}^{-1}$ ), abundant resources, low cost and environmental friendliness.

Metal organic frameworks (MOFs), a class of crystalline sponge-like materials formed by joining metal nodes/clusters to organic linkers, have promising applications due to their excellent specific surface area, tunable pore size and high electrical conductivity [14-16]. By calcining the carbon cloth at high temperatures to produce a large number of pores, it is possible to provide active centres for the homogeneous growth of  $\text{MnO}_2$ , thus permitting high quality loading and full utilization of  $\text{MnO}_2$ , as well as rapid electron/ion transfer. In addition to mass density, the crystal structure, morphology and ionic conductivity of  $\text{MnO}_2$  also influence its electrochemical capacity. Previous studies have confirmed that hydrous sodium manganite  $\text{MnO}_2$  with a layered structure has good electrical and ionic conductivity, as well as chemical stability.

Herein, a two-step hydrothermal approach has been explored to the preparation of (Ni)MOF- $\text{MnO}_2$ //pCC composites, in which (Ni)MOF sheets with abundant micropores and high specific surface area are penetrated with thorn-shaped  $\text{MnO}_2$  while the latter is anchored on the skeletons of porous carbon cloth (pCC). The pCC plays roles as reductive agent and also substrates for the homogeneous growth of  $\text{MnO}_2$ . The rational combination of these three parts ensures good kinetics of electron transport and ion diffusion within the composite electrode. As a result, the (Ni)MOF- $\text{MnO}_2$ //pCC-3 composite electrode shows a high specific capacity of  $1780 \text{ mF cm}^{-2}$  at  $4 \text{ mA cm}^{-2}$ .

## 2. EXPERIMENTAL SECTION

### 2.1. Synthesis of pCC

pCC is prepared from CC by high temperature treatment. Briefly, commercial CC was heated to  $1000^\circ\text{C}$  at a rate of  $5^\circ\text{C}/\text{min}$  in industrial nitrogen, kept for 1 h, and after natural cooling, the obtained pCC was washed several times with deionized water, and then dried by blasting. Dry in a box at  $60^\circ\text{C}$  for 6h.

### 2.2. Synthesis of $\text{MnO}_2$ //pCC

Firstly, 1mmol of  $\text{KMnO}_4$  was dissolved in 5ml of deionized water under ultrasonic dispersion for 15 minutes, then the solution was added to 80 ml of deionized water, the above solution was transferred to a 100 mL Teflon-lined stainless steel reactor and sealed, then a  $1*2\text{cm}$  piece of pCC was immersed in the  $\text{KMnO}_4$  solution and the sealed autoclave was hydrothermally heated at  $85^\circ\text{C}$  for 6 hours. Finally, the resulting sample was thoroughly washed with deionized water and anhydrous ethanol several times and then dried in a blast drying oven at  $70^\circ\text{C}$  for 12h, the resulting in sample labelled as  $\text{MnO}_2$ //pCC.

### 2.3. Synthesis of (Ni)MOF-MnO<sub>2</sub>//pCC-x

(Ni)MOF-MnO<sub>2</sub>//pCC composites were synthesized by hydrothermal growth of (Ni)MOF nanosheets on MnO<sub>2</sub> nano-nanorods. First, 0.16 g of Ni(NO<sub>3</sub>)<sub>2</sub>·6H<sub>2</sub>O and 0.032 g of terephthalic acid (PTA) were dissolved in 20 ml of N, N-dimethylformamide (DMF), respectively. Then Ni(NO<sub>3</sub>)<sub>2</sub>·6H<sub>2</sub>O solution was added dropwise to the PTA solution at a fixed rate of 0.3 ml/min under constant stirring. Afterwards, the Teflon-lined stainless steel reactor containing the mixed solution as well as the MnO<sub>2</sub>//pCC matrix was maintained at 120°C for the designed reaction times (1, 2, 3, 6h). After the stainless steel reactor was cooled to room temperature, the samples were removed, rinsed repeatedly with ethanol and DMF and finally dried in a blast drying oven at 80°C for 6h to obtain (Ni)MOF-MnO<sub>2</sub>//pCC-X composites (the X in the sample name represents the reaction time described above). The mass density of MnO<sub>2</sub> on the pCC of 6.6 mg·cm<sup>-2</sup> has been calculated. Figure 1 shows a schematic diagram of the preparation process of (Ni)MOF-MnO<sub>2</sub>//pCC-X composites.

### 2.4. Characterization

MnO<sub>2</sub>//pCC, (Ni)MOF-MnO<sub>2</sub>//pCC-1, (Ni)MOF-MnO<sub>2</sub>//pCC-2, (Ni)MOF-MnO<sub>2</sub>//pCC-3, (Ni)MOF-MnO<sub>2</sub>//pCC-6 were used as active materials for supercapacitor electrodes in a three-electrode system at room temperature to test their electrochemical storage. The performance was tested and analyzed. The electrochemical performance was tested using 1 mol/L NaSO<sub>4</sub> aqueous solution as the electrolyte, Pt as the counter electrode and Hg/HgO as the reference electrode with a voltage window of 0-1 V. The electrochemical performance was tested using cyclic voltammetry (CV), constant current charge/discharge (GCD) and alternating current impedance (EIS) as well as cycling performance.

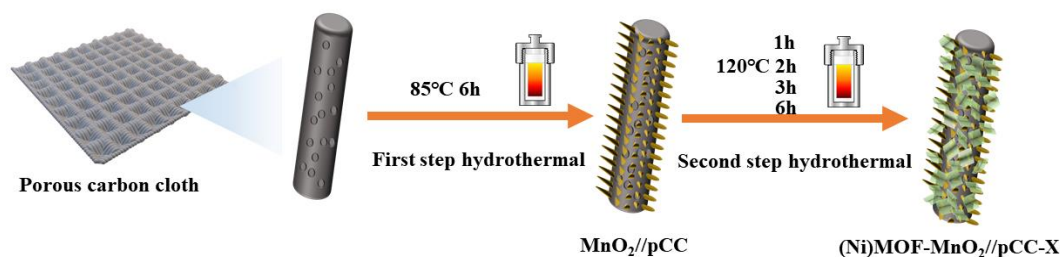


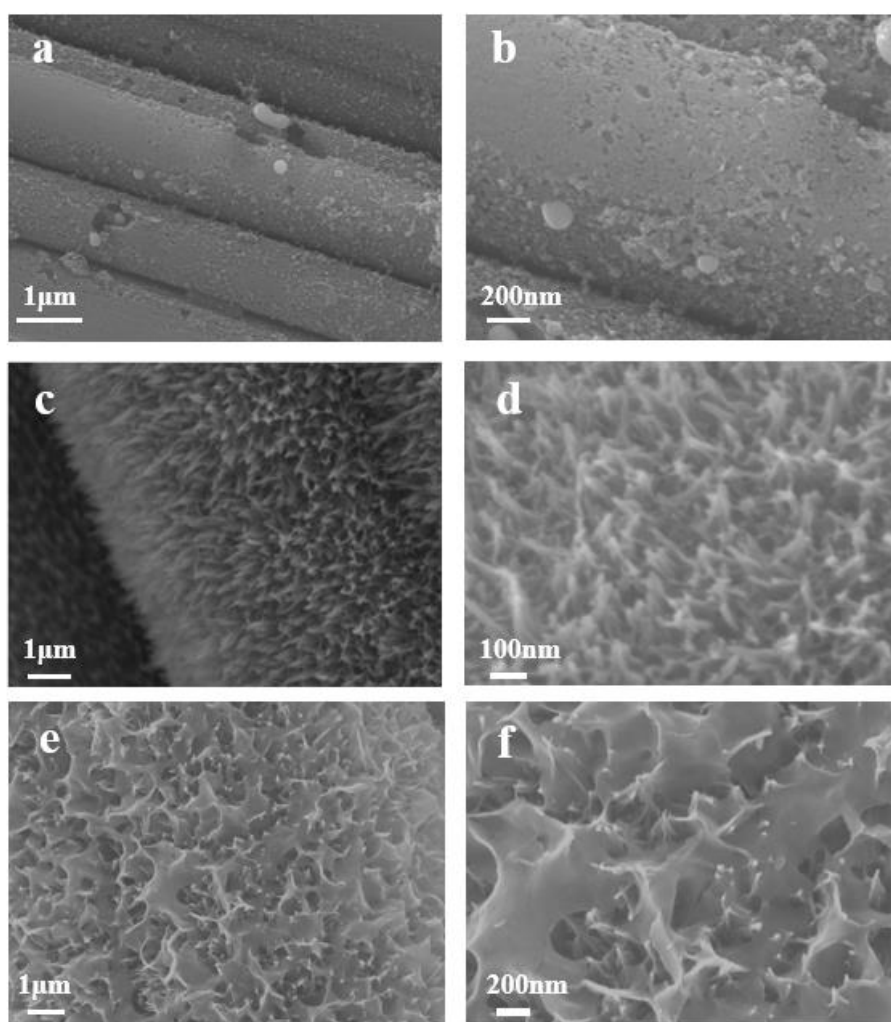
**Figure 1.** The growth process of (Ni)MOF-MnO<sub>2</sub>//pCC-X composites

## 3. RESULTS AND DISCUSSION

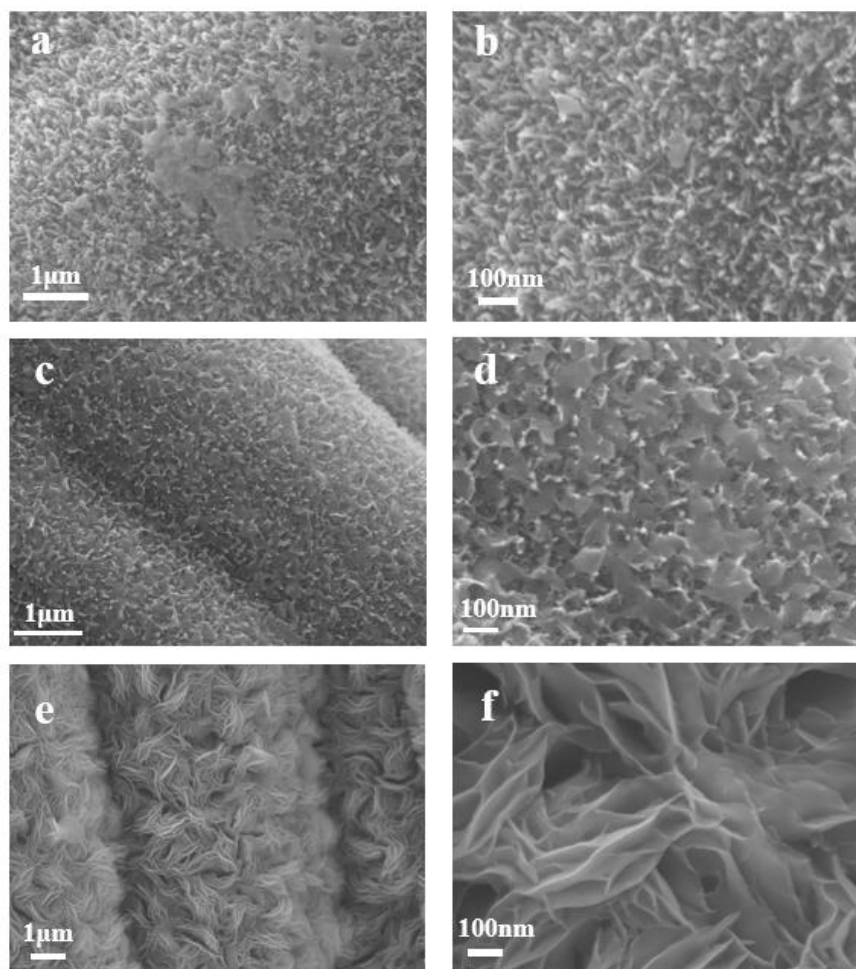
### 3.1. SEM investigations

Figure 2 a and b show SEM images of pCC, the porous carbon cloth (pCC) obtained after the CC was treated at 1000°C. The porous carbon cloth, after the high temperature treatment, possesses a small

number of micropores and a large number of mesopores, providing active sites for the growth of  $\text{MnO}_2$  nano-nanothorns. Figure 2 c and d show SEM images of the  $\text{MnO}_2/\text{pCC}$ , where the hydrothermal treatment in the first step resulted in the uniform growth of large-scale  $\text{MnO}_2$  nano-nanothorns along the porous surface of the nanofibres, which were found to be interconnected in a nanoneedle-like structure by close observation. Figure 2 e and f show SEM images of  $(\text{Ni})\text{MOF-MnO}_2/\text{pCC-3}$ , at which point it can be seen that the flakes of  $(\text{Ni})\text{MOF}$  are formed a large-scale mesh structure and are very homogeneous, in which the needle-like  $\text{MnO}_2$  nano-nanothorns protrudes through the gaps in the mesh  $(\text{Ni})\text{MOF}$  flakes, thus increasing the specific surface area of the  $(\text{Ni})\text{MOF-MnO}_2/\text{pCC-3}$  composite and allowing the material to be further fully exposed to the electrolyte ions and achieve a faster response rate. This also confirms that there is a significant synergistic effect between the composite structures, as mentioned earlier.



**Figure 2.** Low and high magnification SEM images of pCC (a, b),  $\text{MnO}_2/\text{pCC}$  (c, d), and  $(\text{Ni})\text{MOF-MnO}_2/\text{pCC-3}$  (e, f).



**Figure 3.** Low and high magnification SEM images of (Ni)MOF-MnO<sub>2</sub>//pCC-1(a, b), MnO<sub>2</sub>//pCC-2 (c, d), and (Ni)MOF-MnO<sub>2</sub>//pCC-6 (e, f).

Figure 3 a and b show SEM images of (Ni)MOF-MnO<sub>2</sub>//pCC-1. After one hour of hydrothermal heating in the second step, a small portion of (Ni)MOF was found to appear on the surface of the MnO<sub>2</sub> nanothorns, at which point some areas of flaky (Ni)MOF had linked together to form small-scale MOF networks covering the MnO<sub>2</sub> nano-nanothorns. Figure 3 c and d show the SEM images of (Ni)MOF-MnO<sub>2</sub>//pCC-2, It can be found that with the increase of hydrothermal time, (Ni)MOF has been able to form a certain scale of uniform flakes covering the MnO<sub>2</sub> nano-nanothorns, but not a large scale mesh, (Ni)MOF flakes are still not continuous. It is worth noting that one is able to control the growth of the (Ni)MOF sheets by adjusting the time of the hydrothermal reaction. Figure 3 e and f show SEM images of (Ni)MOF-MnO<sub>2</sub>//pCC-6. At the hydrothermal reaction time of 6h, the (Ni)MOF forms closely packed nanoflakes completely covering the MnO<sub>2</sub> nano-nanothorns, at which point the presence of MnO<sub>2</sub> is no longer visible, a situation that affects the rate of electron transport.

## 3.2. TEM investigations

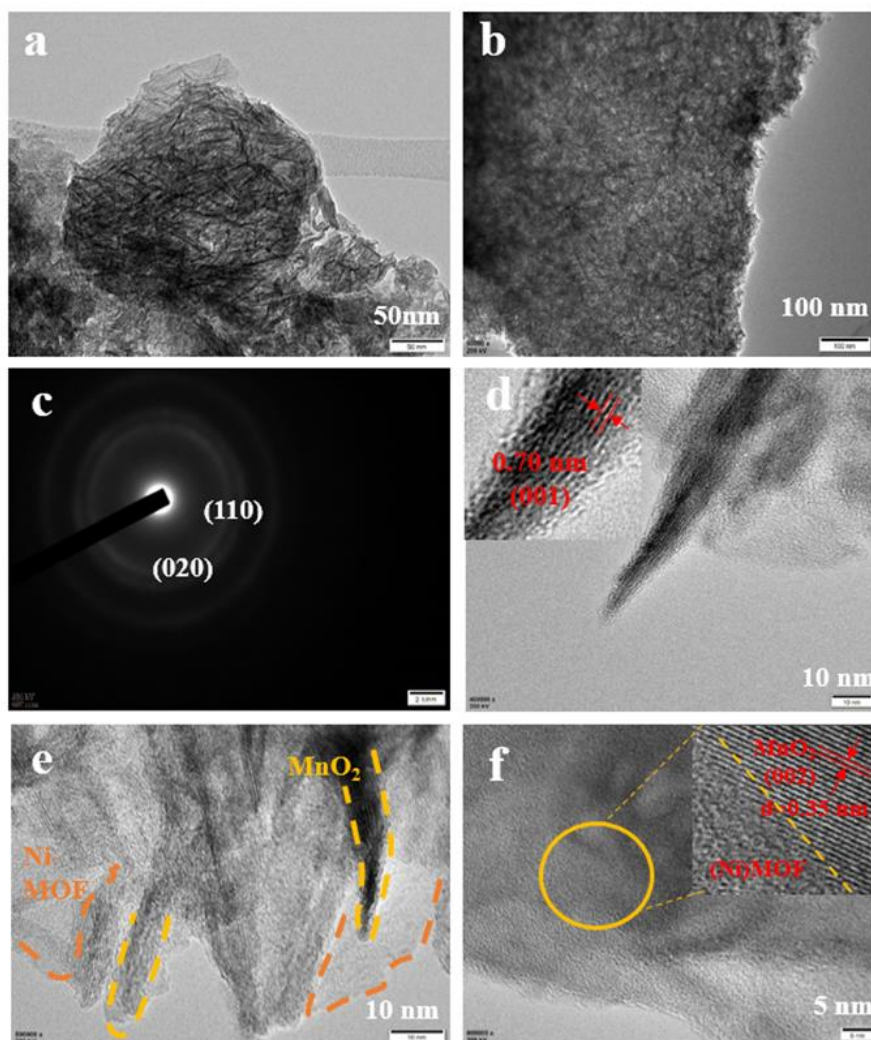


**Figure 4.** (a)(b) Low-resolution TEM image of (Ni)MOF-MnO<sub>2</sub>//pCC-3, (c) Selected area electron diffraction pattern of (Ni)MOF-MnO<sub>2</sub>//pCC-3, (d)(e)(f) High-resolution TEM image of (Ni)MOF-MnO<sub>2</sub>//pCC-3

The morphology and microstructure of the (Ni)MOF-MnO<sub>2</sub>//pCC-3 composites were observed by transmission electron microscopy (TEM) on specimens scraped from the carbon fibres. As shown in Figure 4.a, the large area of (Ni)MOF is uniformly covered on top of the MnO<sub>2</sub> nano-nanorods, and its open lamellar structure facilitates the full penetration of the electrolyte in the reaction, making the reaction more complete. As shown in Fig 4.b (Ni)MOF-MnO<sub>2</sub>//pCC-3 low magnification TEM image, we can clearly see the porous structure of (Ni)MOF covered with MnO<sub>2</sub>. From the high magnification TEM images of Fig 4.d, e (Ni)MOF-MnO<sub>2</sub>//pCC-3, it can be noticed that the MnO<sub>2</sub> nano-nanorods penetrate the MOF sheet, which can greatly enhance the electrical connection and facilitate fast electron transport within the hybrid electrode. As shown in Fig 4.f the high resolution TEM images clearly show the interface between MOF and MnO<sub>2</sub> in the composite and clearly reveal the lattice edges of MnO<sub>2</sub>. The calculated lattice spacings of  $d=0.35$  nm and  $d=0.76$  nm can refer to the (0,0,2) and (0,0,1) crystal

planes of  $\text{MnO}_2$ , respectively, which is consistent with the results measured in the XRD pattern above; in addition, as shown in Figure 4.c selected area diffraction reveals two concentric rings that can refer to the (1,1,0) and (0,2,0) crystal planes of  $\text{MnO}_2$ , respectively. It is worth mentioning that HRTEM was unable to obtain clear lattice stripes from 2D Ni-MOF nanosheets, probably due to the intrinsic characteristics of Ni-MOF, as similarly reported in earlier publications [17-19], and the unstable nature of Ni-MOF. MOF under strong electron beam irradiation makes imaging more difficult.

### 3.3. XRD measurements

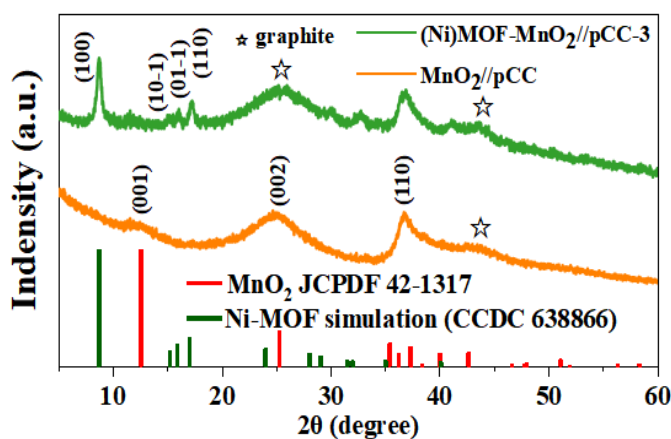


**Figure 5.** patterns of  $\text{MnO}_2//\text{pCC}$  and  $(\text{Ni})\text{MOF-MnO}_2//\text{pCC-3}$

The phase properties of  $\text{MnO}_2//\text{pCC}$  and  $(\text{Ni})\text{MOF-MnO}_2//\text{pCC-3}$  as shown in Figure 5 have also been characterised by X-ray diffraction (XRD) pattern analysis. It is known that the two diffraction peaks marked with star at  $2\theta$  at  $26^\circ$  and  $43^\circ$  are from carbon cloth. The two curves with diffraction peaks at  $2\theta = 12^\circ$ ,  $25^\circ$  and  $37^\circ$  are well corresponded to the (0, 0, 1), (0, 0, 2) and (1, 1, 0) crystal planes and the XRD pattern corresponds exactly to the  $\text{MnO}_2$  phase of hydrous sodalite (JCPDS 42-1317). It is noteworthy that the diffraction peak at  $25^\circ$  overlaps with the  $26^\circ$  diffraction peak from carbon cloth, the reason for this being the  $\text{MnO}_2$  phase of hydrous sodium manganese ore, which is known from the valence state of Mn in the later XPS analysis. In the XRD pattern of  $(\text{Ni})\text{MOF-MnO}_2//\text{pCC-3}$ , several peaks can also be observed at  $8.7^\circ$ ,  $15.2^\circ$ ,  $15.9^\circ$  and  $17^\circ$ , which can be corresponded to the diffraction peaks of Ni-MOF at (1, 0, 0), (1, 0, -1), (0, 1, -1) and (1, 1, 0) (CCDC 638866). Thus, the XRD pattern of  $(\text{Ni})\text{MOF-MnO}_2//\text{pCC-3}$  is a superposition of the phase of  $\text{MnO}_2$  and the phase of (Ni)MOF, indicating the co-existence of the two components. Thus, the XRD characterisation results demonstrate the successful preparation of  $(\text{Ni})\text{MOF-MnO}_2//\text{pCC}$  composites.

## 3.4. XPS measurements

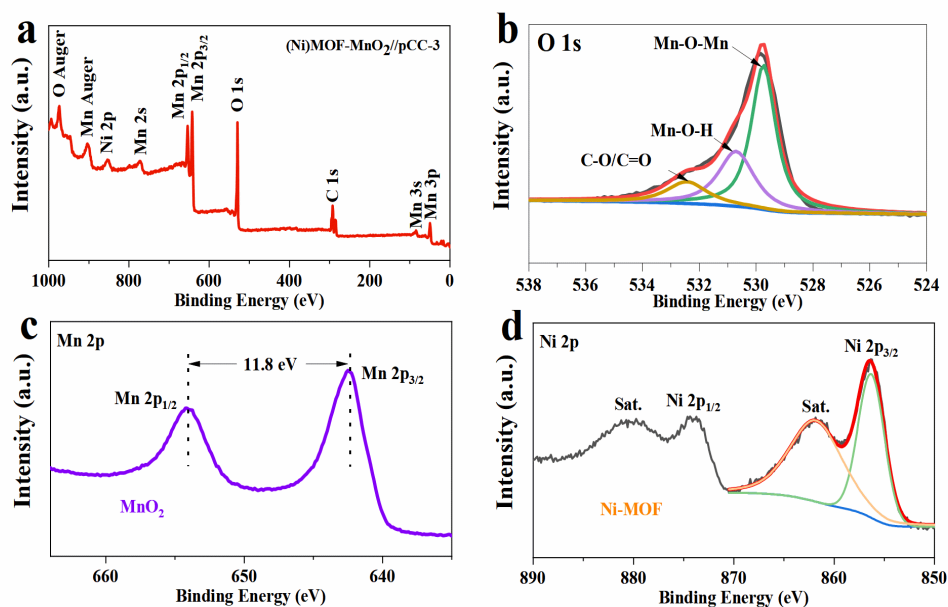


**Figure 6.** XRD patterns of  $\text{MnO}_2//\text{pCC}$  and  $(\text{Ni})\text{MOF-MnO}_2//\text{pCC-3}$  (panel a), XPS survey spectra of  $(\text{Ni})\text{MOF-MnO}_2//\text{pCC-3}$  (b), High resolution XPS spectra at the Mn2p (c) and Ni2p (d) regions.

The chemical composition of the  $(\text{Ni})\text{MOF-MnO}_2//\text{pCC-3}$  composites and the valence states of the elements contained were characterised by X-ray photoelectron spectroscopy (XPS) techniques. The full XPS spectrum of  $(\text{Ni})\text{MOF-MnO}_2//\text{pCC-3}$ , as shown in Figure 6a exhibits characteristic peaks of Mn, Ni, C and O, which is in agreement with the results obtained after analysis in the XRD pattern. As shown in Figure 6b the O 1s high resolution spectrum can be fitted to three peaks, indicating the presence of three types of oxygen states. The peak at 529.7 eV is the Mn-O-Mn bond in  $\text{MnO}_2$ , the peak at 530.7 eV is the Mn-O-H bond in  $\text{MnO}_2$ , usually associated with hydroxylation of the metal surface, and the peak at 532.6 eV represents the C-O/C=O bond. As shown in Figure 6c a high resolution XPS spectrum of Mn 2p, the two peaks centred at 642.5 eV and 654.0 eV correspond to Mn 2p<sub>1/2</sub> and Mn 2p<sub>3/2</sub>. After deconvolution the two peaks at 642.6 eV and 654.4 eV are attributed to  $\text{Mn}^{2+}$ , which also proves that the characteristic peak of  $\text{MnO}_2$  is indeed present at  $25^\circ$  in the XRD pattern. This indicates that the product produced is the  $\text{MnO}_2$  phase in aqueous sodium manganese ore. The spin energy separation was 11.8 eV, which is consistent with previous reports on  $\text{MnO}_2$  [20-23]. A high resolution XPS spectrum of Ni 2p is shown in Figure 6d with the spectrum showing two peaks centred at 873.6 eV and 856.2 eV corresponding to Ni 2p<sub>1/2</sub> and Ni 2p<sub>3/2</sub>, accompanied by two satellite peaks at 880.1 eV and 861.5 eV, and after deconvolution, two peaks at 874.3 eV and 856.0 eV attributed to  $\text{Ni}^{2+}$ .

## 3.5. Porosity characters

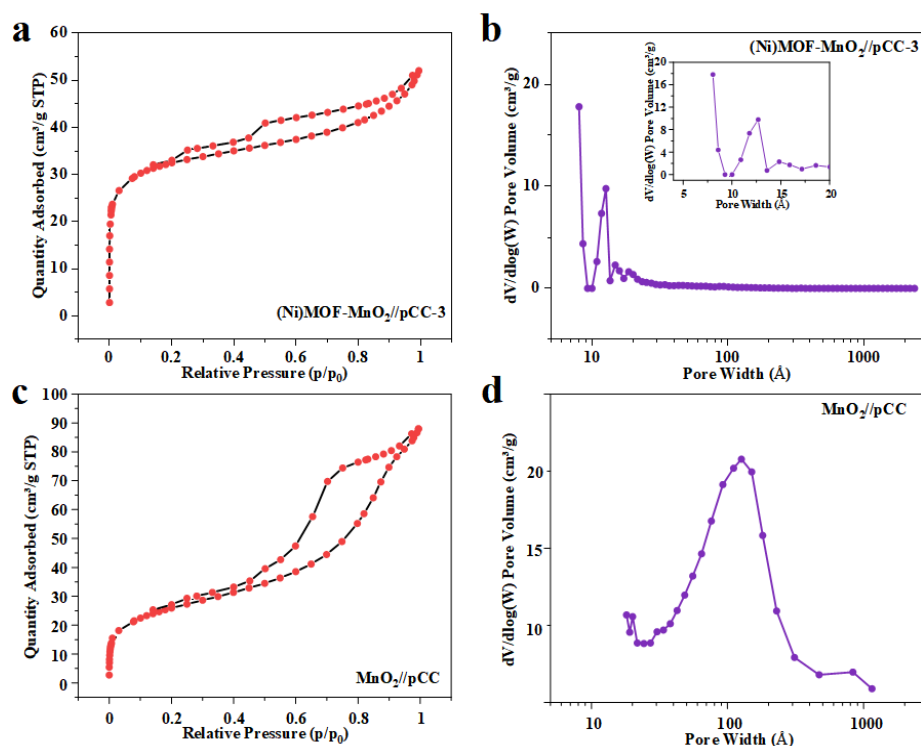


**Figure 7.** N<sub>2</sub> sorption isotherms (a) the pore size distribution curves (b) of (Ni)MOF-MnO<sub>2</sub>//pCC-3. N<sub>2</sub> sorption isotherms (c) the pore size distribution curves (d) of (Ni)MOF-MnO<sub>2</sub>//pCC

We used nitrogen adsorption/desorption curves to analyze the porosity of the (Ni)MOF-MnO<sub>2</sub>//pCC-3 samples. As shown in Figure 7a (Ni)MOF-MnO<sub>2</sub>//pCC-3, roughly shows a Type IV isotherm associated with an H3-type hysteresis line. At the beginning of the adsorption, the isotherm increases dramatically, indicating the presence of a large number of microporosity, and as the relative pressure continues to rise, the (Ni)MOF-MnO<sub>2</sub>//pCC-3 isotherm shows a hysteresis loop in the p/p<sub>0</sub> interval of 0.5-0.9, which contains a small amount of mesopores, and the BET model analysis shows that the specific surface area is 107.4 m<sup>2</sup>/g. The adsorption pore size distribution curve fitted by the DFT model is shown in Figure 7b, with an average pore size of 0.8 nm.

Figure 7c shows the nitrogen adsorption/desorption curve of the MnO<sub>2</sub>//pCC sample as a type IV isotherm associated with the H3 type hysteresis line, from which it can be seen that it contains only a small number of micropores compared to the (Ni)MOF-MnO<sub>2</sub>//pCC-3 sample. The adsorption pore size distribution curve fitted by the BJH model is shown in Figure 7d, with an average pore size of 7.2 nm. The specific surface area and average pore size parameters of the two materials are shown in Table 1.

**Table 1.** The specific surface area and average pore width of MnO<sub>2</sub>//pCC-3 and (Ni)MOF-MnO<sub>2</sub>//pCC-3

Sample	Surface area (m <sup>2</sup> ·g <sup>-1</sup> )	Pore Volume (m <sup>3</sup> ·g <sup>-1</sup> )
MnO <sub>2</sub> //pCC-3	81.5	7.2
(Ni) MOF-MnO <sub>2</sub> //pCC-3	107.4	0.8

### 3.6. Electrochemical properties

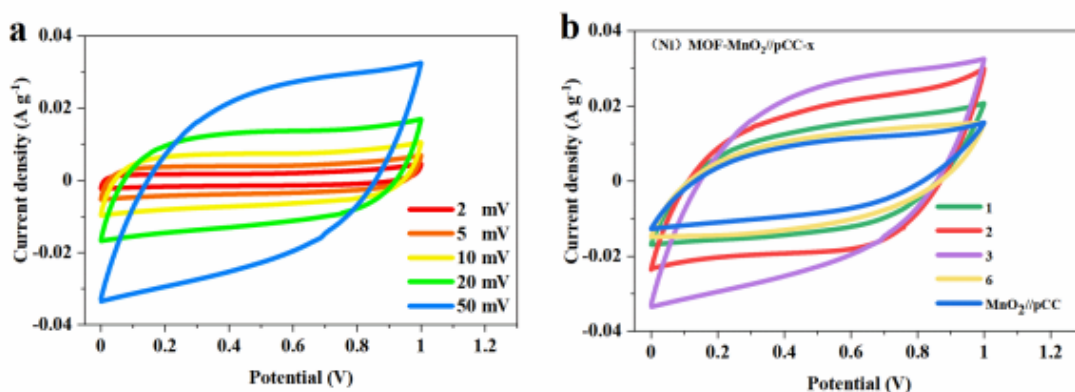
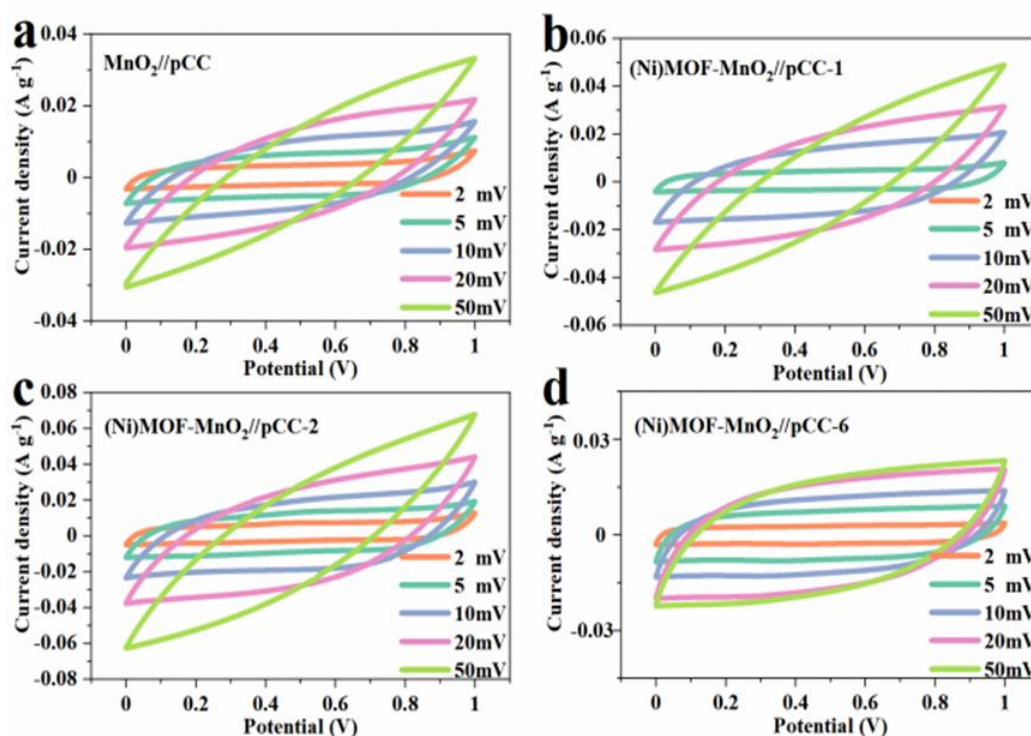
**Figure 8.** (a) The CV curves of MnO<sub>2</sub>//pCC-3 at different scan rates. (b) The CV curves of these MnO<sub>2</sub>//pCC-x composites at 50 mV.

Figure 8a shows the CV curves of MnO<sub>2</sub>//pCC-3 at different scan rates. A comparison of the CV curves for the MnO<sub>2</sub>//pCC sample and the MnO<sub>2</sub>//pCC and (Ni)MOF samples hydrothermally heated for 1h, 2h, 3h and 6h respectively is shown in Figure 8b. The images obtained at a current density of 50 mV, as can be observed through the plots, show a diamond shape for all four samples, indicating that such supercapacitors are reversible, which is also consistent with the shape of the CV curve for pseudocapacitor supercapacitors. Compared with MnO<sub>2</sub>//pCC, (Ni)MOF-MnO<sub>2</sub>//pCC-1, (Ni)MOF-MnO<sub>2</sub>//pCC-2 and (Ni)MOF-MnO<sub>2</sub>//pCC-6, the (Ni)MOF-MnO<sub>2</sub>//pCC-3 composite exhibits the largest peak current density and also has the largest area of the CV curve of the four materials. The (Ni)MOF-MnO<sub>2</sub>//pCC-3 composite exhibits the largest peak current density and the largest area of the CV curve of the four materials. The capacitive performance was also the best of the four materials. The peak current density of the samples increased with the increase of the hydrothermal time because: (Ni)MOF gradually formed a uniform mesh structure covering the MnO<sub>2</sub> nano-nanorhorns with the increase of the hydrothermal time, but when the hydrothermal time reached 6h, the peak current density became smaller instead, because the sheet-like (Ni)MOF had completely covered the MnO<sub>2</sub> nano-nanorhorns by the time the hydrothermal time was 6h. nano-nanorhorns, which affects the electrochemical activity of MnO<sub>2</sub>. However, since (Ni)MOF itself has a certain capacity, and the capacity of (Ni)MOF is higher than that of MnO<sub>2</sub>, it exhibits a larger CV closure area than MnO<sub>2</sub>//pCC.

Of particular note, the composite of (Ni)MOF-MnO<sub>2</sub>//pCC-3 exhibits significantly increased CV closure area and peak current density compared to pristine MnO<sub>2</sub>//pCC-3 and (Ni)MOF-MnO<sub>2</sub>//pCC-6, reflecting the fact that the (Ni)MOF nanosheets in the composite can provide much higher capacity than

pure (Ni)MOF nanosheets. This reflects the fact that (Ni)MOF nanosheets in the composites can provide much higher capacity than pure (Ni)MOF nanosheets. This confirms that there is a significant synergistic effect between the composite structures. This is consistent with the conclusions in previous report[24].



**Figure 9.** The CV curves of MnO<sub>2</sub>//pCC (a), MnO<sub>2</sub>//pCC-1 (b), MnO<sub>2</sub>//pCC-3 (c) and MnO<sub>2</sub>//pCC-6 (d) at different scan rates.

The CV curves for MnO<sub>2</sub>//pCC, (Ni)MOF-MnO<sub>2</sub>//pCC-1, (Ni)MOF-MnO<sub>2</sub>//pCC-2, (Ni)MOF-MnO<sub>2</sub>//pCC-3, (Ni)MOF-MnO<sub>2</sub>//pCC-6 at sweep rates of 2, 5, 10, 20 and 50 mV are shown in Figure 9. According to the CV curves in Figure 9, the specific capacitance decreases as the current density increases, which shows that the specific capacitance of the electrode material is influenced by the sweep speed, and the specific capacitance of the electrode decreases significantly with the increase of the sweep speed. This is because increasing the sweep speed directly affects the diffusion rate of Na<sup>+</sup> in MnO<sub>2</sub>, and at a higher sweep rate, Na<sup>+</sup> can only approach the outer surface of the electrode, so the micro-pores inside the active material contribute less to the capacitance and the specific capacitance is low.

Figure 10a shows the GCD curves of MnO<sub>2</sub>//pCC-3 at different current density. Figure 10b shows the constant current measured for MnO<sub>2</sub>//pCC, (Ni)MOF-MnO<sub>2</sub>//pCC-1, (Ni)MOF-MnO<sub>2</sub>//pCC-2, (Ni)MOF-MnO<sub>2</sub>//pCC-3, (Ni)MOF-MnO<sub>2</sub>//pCC-6 at a voltage window of 0-1V and a current density of 4mA/cm<sup>2</sup> Charge and discharge curves. It can be seen from Figure 8b that all curves have a very slight drop in voltage due to the internal resistance of MnO<sub>2</sub> itself. The capacity of (Ni)MOF-MnO<sub>2</sub>//pCC-3 is larger than the other samples, which can also be found in the SEM images. Based on the curves it can be observed that all these four samples show a high degree of symmetry in their charge and discharge times and it can be inferred that the resulted materials can maintain very good reversibility and

conductivity. Table 2 shows the comparison between the results of this work and those previously reported in other work.

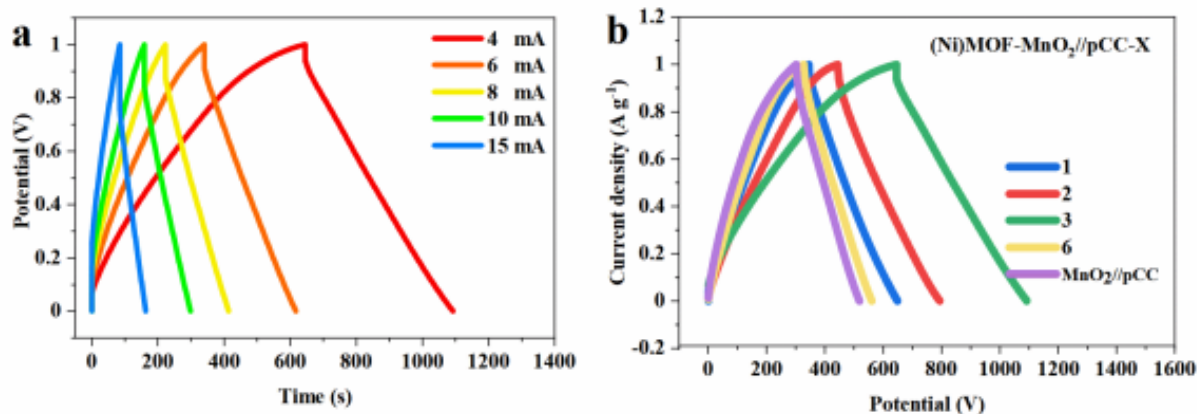


**Figure 10.** (a) The GCD curves of MnO<sub>2</sub>//pCC-3 at different current density. (b) The GCD curves of these MnO<sub>2</sub>//pCC-x composites at 4 mA/cm<sup>2</sup>

The capacity value of (Ni)MOF-MnO<sub>2</sub>//pCC-3 is quite remarkable in comparison to those of previously documented composites. For instance, MnO<sub>2</sub>/Ni foam (150 mF/cm<sup>2</sup> at 2 mA/cm<sup>2</sup>)[25], MnO<sub>2</sub>/CNT(337 mF/cm<sup>2</sup> at 2 mA/cm<sup>2</sup>)[26], 3D graphene/CNT/MnO<sub>2</sub> (87 mF/cm<sup>2</sup> at 4 mA/cm<sup>2</sup>)[27], MnO<sub>2</sub>/Graphene/Ni foam (245 mF/cm<sup>2</sup> at 3 mA/cm<sup>2</sup>)[28], Self-branched MnO<sub>2</sub>(232 mF/cm<sup>2</sup> at 2 mA/cm<sup>2</sup>)[29], N-doped graphene/MnO<sub>2</sub> (217 mF/cm<sup>2</sup> at 2 mA/cm<sup>2</sup>)[30], and MnO<sub>2</sub>/CNTs (387 mF/cm<sup>2</sup> at 2 mA/cm<sup>2</sup>)[31].

**Table 2.** Comparison of electrochemical performance for (Ni)MOF-MnO<sub>2</sub>//pCC-3 with previous reported results.

Material	Capacity	Current density	Electrolyte	Ref.
(Ni)MOF-MnO <sub>2</sub> //pCC-3	1780 mF/cm <sup>2</sup>	4 mA/cm <sup>2</sup>	1 M Na <sub>2</sub> SO <sub>4</sub>	This work
MnO <sub>2</sub> /Ni foam	150 mF/cm <sup>2</sup>	2 mA/cm <sup>2</sup>	0.5 M Na <sub>2</sub> SO <sub>4</sub>	24
MnO <sub>2</sub> /CNT	337 mF/cm <sup>2</sup>	1 mA/cm <sup>2</sup>	1 M Na <sub>2</sub> SO <sub>4</sub>	25
3D graphene/CNT/MnO <sub>2</sub>	87 mF/cm <sup>2</sup>	4 mA/cm <sup>2</sup>	1 M Na <sub>2</sub> SO <sub>4</sub>	26
MnO <sub>2</sub> /Graphene/Ni foam	245 mF/cm <sup>2</sup>	3 mA/cm <sup>2</sup>	0.5 M Na <sub>2</sub> SO <sub>4</sub>	27
Self-branched MnO <sub>2</sub>	232 mF/cm <sup>2</sup>	2 mA/cm <sup>2</sup>	1 M Na <sub>2</sub> SO <sub>4</sub>	28
N-doped graphene/MnO <sub>2</sub>	217 mF/cm <sup>2</sup>	2 mA/cm <sup>2</sup>	0.5 M Na <sub>2</sub> SO <sub>4</sub>	29
MnO <sub>2</sub> /CNTs	387 mF/cm <sup>2</sup>	2 mA/cm <sup>2</sup>	1 M Na <sub>2</sub> SO <sub>4</sub>	30

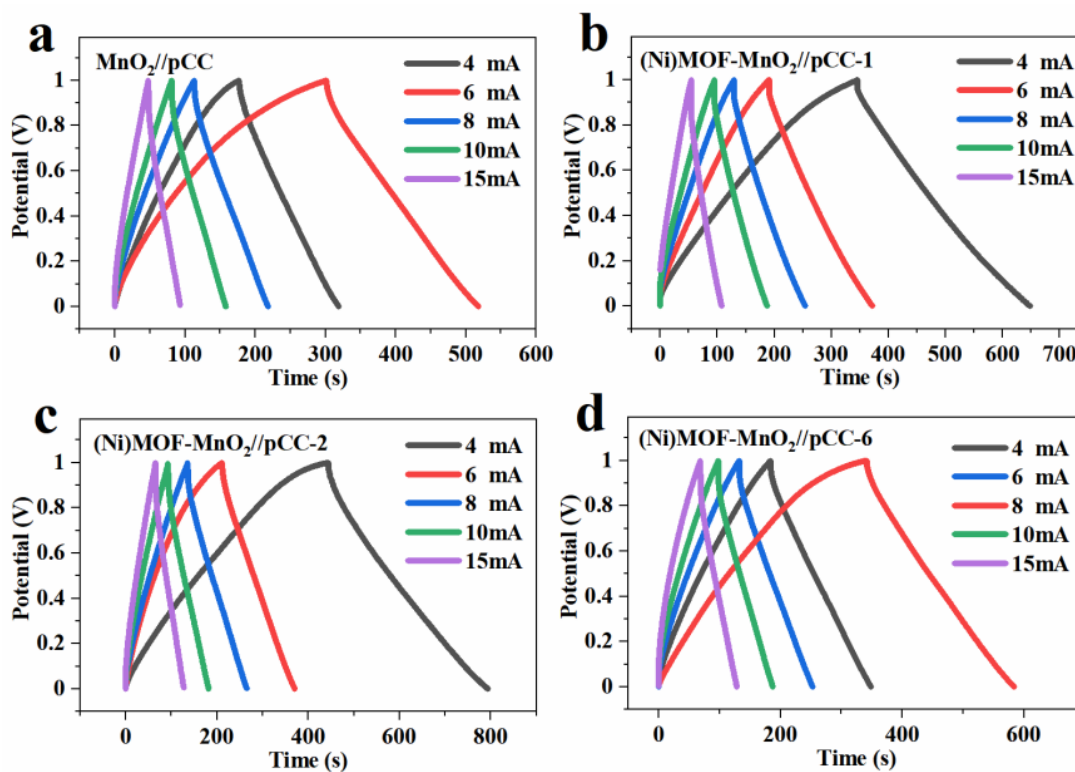


**Figure 11.** The GCD curves of (a)  $\text{MnO}_2//\text{pCC}$  (b)  $(\text{Ni})\text{MOF-MnO}_2//\text{pCC-1}$ , (c)  $(\text{Ni})\text{MOF-MnO}_2//\text{pCC-2}$ , and (d)  $(\text{Ni})\text{MOF-MnO}_2//\text{pCC-6}$  at different current densities.

As shown in Figure 11, the GCD of  $\text{MnO}_2//\text{pCC}$ ,  $(\text{Ni})\text{MOF-MnO}_2//\text{pCC-1}$ ,  $(\text{Ni})\text{MOF-MnO}_2//\text{pCC-2}$ , and  $(\text{Ni})\text{MOF-MnO}_2//\text{pCC-6}$  at current densities of 4, 6, 8, 10 and 15 mA. According to the GCD curves in Fig. S4, the charging and discharging curves of the composite electrodes at different current densities basically show a symmetrical triangle, and the electrode potential varies linearly with time, showing good capacitive characteristics. The discharge specific capacitance of the electrode material decreases when the current density increases, because when the current density is small, the specific capacitance of the supercapacitor is contributed by the surface of the electrode as well as the active material inside, and the utilization rate of the active material is higher and the charging and discharging is more complete. As the current density increases, only the active material on the surface of the electrode material undergoes an electrode reaction, leading to a decrease in the discharge specific capacitance, which is consistent with the results obtained by cyclic voltammetry tests.

Figure 12a shows the comparison of the multiplicity performance obtained from the multiplicity tests done for  $\text{MnO}_2//\text{pCC}$ ,  $(\text{Ni})\text{MOF-MnO}_2//\text{pCC-1}$ ,  $(\text{Ni})\text{MOF-MnO}_2//\text{pCC-2}$ ,  $(\text{Ni})\text{MOF-MnO}_2//\text{pCC-3}$ ,  $(\text{Ni})\text{MOF-MnO}_2//\text{pCC-6}$  at different current densities. By looking at the curves it can be noticed that as the power density increases, there is a significant decrease in the energy density. It is clear that the energy densities of all four samples produced are much higher than those of conventional supercapacitors, and their power densities are also higher than those of batteries. In particular, the energy and power densities of the  $(\text{Ni})\text{MOF-MnO}_2//\text{pCC-3}$  composite are much higher compared to the other samples, with a calculated specific capacitance of 376 F/g at a current density of 1 A/g and an area capacitance of 1780 mF/cm<sup>2</sup> at a current density of 4 mA/cm<sup>2</sup>. This also proves that the  $(\text{Ni})\text{MOF-}$

MnO<sub>2</sub>//pCC-3 composite is ideal for use as a supercapacitor. (Ni)MOF-MnO<sub>2</sub>//pCC-3 composite is an ideal cathode material for supercapacitors.

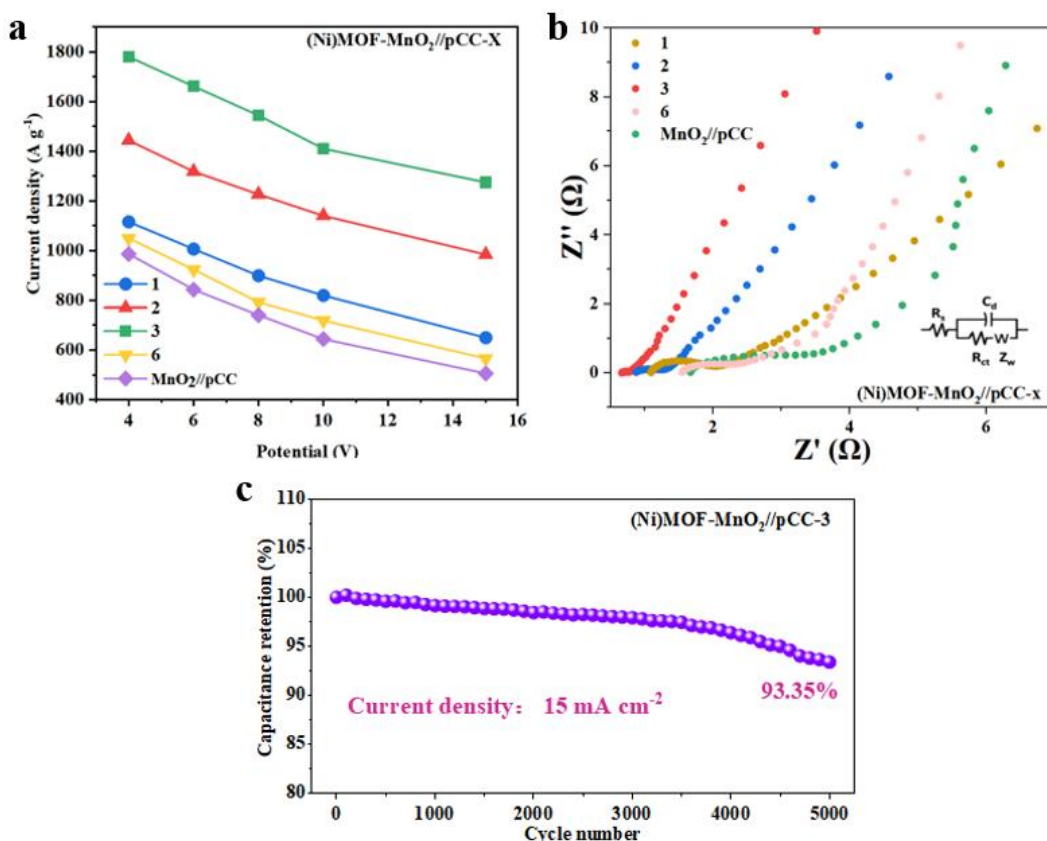


**Figure 12.** (a) The ragone plots comparison of MnO<sub>2</sub>//pCC and (Ni)MOF-MnO<sub>2</sub>//pCC-X at different current density. (b) The EIS spectrum of MnO<sub>2</sub>//pCC, (Ni)MOF-MnO<sub>2</sub>//pCC-X. (c) The cycling performance of (Ni)MOF-MnO<sub>2</sub>//pCC-3 at a current density of 15 mA/cm<sup>2</sup>

The Nyquist plots of the electrochemical impedance spectra (EIS) spectra of these five electrodes are shown in Figure 12b. All these plots are characterized by semicircles and diagonal lines in the high and low frequency regions, which are thought to be related to the charge transfer resistance (R<sub>s</sub>) and Warburg impedance (Z<sub>w</sub>) at the electrode/electrolyte interface, with the intercept with the real axis indicating the equivalent series resistance (R<sub>ct</sub>) [32,33]. From the figure, we can see that (Ni)MOF-MnO<sub>2</sub>//pCC-3 has the smallest transfer resistance and therefore the combined advantages of fast electron transport and ion diffusion kinetics can well explain the enhanced electrochemical performance of the (Ni)MOF-MnO<sub>2</sub>//pCC-3 hybrid electrode.

As can be seen in Figure 12c, (Ni)MOF-MnO<sub>2</sub>//pCC-3 can maintain an initial capacitance of 93.35% at a current density of 15 mA/cm<sup>2</sup> after 5000 charge/discharge cycles, indicating that its excellent long cycle performance is attributed to the (Ni)MOF covering the MnO<sub>2</sub> nanothorns, which has a good synergistic effect. The good synergistic effect is also due to the rich microporous structure of the (Ni)MOF, which provides a channel for ion mass transfer.

#### 4. CONCLUSIONS

(Ni)MOF-MnO<sub>2</sub>//pCC composites were fabricated using a simple two-step hydrothermal method. The MnO<sub>2</sub> nanothorns is the main capacity providing material, and the large-scale mesh of (Ni)MOF is covered on top of the MnO<sub>2</sub> nano-nanothorns to increase its electrical conductivity and also increase the specific surface area also providing abundant micro-pores. Experimental analysis reveals that control of the morphology of the (Ni)MOF-MnO<sub>2</sub>//pCC-X composites can be achieved by controlling the time of the hydrothermal reaction, and their electrochemical energy varies. Among them, (Ni)MOF-MnO<sub>2</sub>//pCC-3 was used as a cathode material for supercapacitors exerting excellent electrochemical performance, providing a high specific capacitance of 376 F/g at a current density of 1 A/g. In addition, the electrode exhibited satisfactory cycling stability by maintaining 93.35% specific capacitance over the initial capacitance after 5000 consecutive charge/discharge cycles. This environmentally friendly and cost-effective preparation method shows promise in the development of high-performance composites for advanced energy storage devices.

#### ACKNOWLEDGEMENTS

This work is supported by the National Key R&D Program of China (2021YFB2400200) and the Natural Science Foundation of Shandong Province (ZR2020ME057).

#### References

1. V. Subramanian, H.W. Zhu, B.Q. Wei, *J. Power Sources*, 159 (2006) 361
2. Y. Li, H.Q. Xie, J.F. Wang, L.F. Chen, *Materials Letters*, 65 (2011) 403
3. Y. Zhang, H. Feng, X.B. Wu, L.Z. Wang, A.Q. Zhang, T.C. Xia, H.C. Dong, X.F. Li, L.S. Zhang, *International Journal of Hydrogen Energy*, 34 (2009) 4889
4. A. Rudge, J. Davey, I. Raistrick, S. Gottesfeld, J.P. Ferraris, *J. Power Sources*, 47 (1994) 89
5. R.B. Rakhi, W. Chen, D.K. Cha, H.N. Alshareef, *Journal of Materials Chemistry*, 21 (2011) 16197
6. B. Fang, Y.Z. Wei, K. Maruyama, M. Kumagai, *Journal of Applied Electrochemistry*, 35 (2005) 229
7. W. Chen, Z.L. Fan, L. Gu, X.H. Bao, C.L. Wang, *Chemical Communications*, 46 (2010) 3905
8. Q. Cheng, J. Tang, J. Ma, H. Zhang, N. Shinya, L.C. Qin, *Carbon*, 49 (2011) 2917
9. Y.G. Wang, Z.D. Wang, Y.Y. Xia, *Electrochimica Acta*, 50 (2005) 5641
10. A. Phuruangrat, T. Thongtem, S. Thongtem, *Materials Letters*, 63 (2009) 1224
11. Y. Ren, L.A. Gao, *Journal of the American Ceramic Society*, 93 (2010) 3560
12. T.L. Lai, Y.L. Lai, J.W. Yu, Y.Y. Shu, C.B. Wang, *Materials Research Bulletin*, 44 (2009) 2040
13. S.K. Meher, G.R. Rao, *J. Power Sources*, 215 (2012) 317
14. W. Du, Y.-L. Bai, J. Xu, H. Zhao, L. Zhang, X. Li, J. Zhang, *J. Power Sources*, 402 (2018) 281
15. H. Furukawa, K.E. Cordova, M. O'Keeffe, O.M. Yaghi, *Science*, 341 (2013) 974
16. H. He, Q. Zhu, Y. Yan, H. W. Zhang, Z. Han, H. Sun, J. Chen, C. P. Li, Z. Zhang, M. Du, *Applied Catalysis B: Environmental*, Volume 302, March 2022, 120840
17. J. Yang, Z. Ma, W. Gao, M. Wei, *Chemistry*, 23 (2017) 631
18. Y. Yan, P. Gu, S. Zheng, M. Zheng, H. Pang, H. Xue, *Journal of Materials Chemistry A*, 4 (2016) 19078
19. C. Zhang, Z. Qi, Z. Kai, Z. Xiao, W.J.R.A. Lei, *RSC Adv*, 8 (2018) 17747
20. F.-X. Ma, L. Yu, C.-Y. Xu, X.W. Lou, *Energy & Environmental Science*, 9 (2016) 862

21. L. Bao, J. Zang, X. Li, *Nano Lett*, 11 (2011) 1215
22. X. Lu, T. Zhai, X. Zhang, Y. Shen, L. Yuan, B. Hu, L. Gong, J. Chen, Y. Gao, J. Zhou, Y. Tong, Z.L. Wang, *Adv Mater*, 24 (2012) 938
23. H. Xu, X. Hu, H. Yang, Y. Sun, C. Hu, Y. Huang, *Advanced Energy Materials*, 5 (2015)
24. G. Li, H. Cai, X. Li, J. Zhang, D. Zhang, Y. Yang, J. Xiong, *ACS Appl Mater Interfaces*, 11 (2019) 37675
25. J. Yang, L.F. Lian, H.C. Ruan, F.Y. Xie, M.D. Wei, *Electrochimica Acta*, 136 (2014) 189
26. J.L. Liu, L.L. Zhang, H.B. Wu, J.Y. Lin, Z.X. Shen, X.W. Lou, *Energy & Environmental Science*, 7 (2014) 3709
27. Y. He, W. Chen, X. Li, Z. Zhang, J. Fu, C. Zhao, E. Xie, *ACS Nano*, 7 (2013) 174
28. T. Zhai, F. Wang, M. Yu, S. Xie, C. Liang, C. Li, F. Xiao, R. Tang, Q. Wu, X. Lu, Y. Tong, *Nanoscale*, 5 (2013) 6790
29. C. Zhu, L. Yang, J.K. Seo, X. Zhang, S. Wang, J. Shin, D. Chao, H. Zhang, Y.S. Meng, H.J. Fan, *Materials Horizons*, 4 (2017) 415
30. Y.C. Liu, X.F. Miao, J.H. Fang, X.X. Zhang, S.J. Chen, W. Li, W.D. Feng, Y.Q. Chen, W. Wang, Y.N. Zhang, *Acs Applied Materials & Interfaces*, 8 (2016) 5251
31. P. Wu, S. Cheng, L. Yang, Z. Lin, X. Gui, X. Ou, J. Zhou, M. Yao, M. Wang, Y. Zhu, M. Liu, *ACS Appl Mater Interfaces*, 8 (2016) 23721.
32. N. Jabeen, Q.Y. Xia, M. Yang, H. Xia, *Acs Applied Materials & Interfaces*, 8 (2016) 6093
33. F. Ning, M. Shao, C. Zhang, S. Xu, M. Wei, X. Duan, *Nano Energy*, 7 (2014) 134

© 2022 The Authors. Published by ESG ([www.electrochemsci.org](http://www.electrochemsci.org)). This article is an open access article distributed under the terms and conditions of the Creative Commons Attribution license (<http://creativecommons.org/licenses/by/4.0/>).